Supporting Information for "Revisiting the 1959 Hebgen Lake earthquake using optical image correlation; new constraints on near-field 3D ground displacement"

Lucia Andreuttiova[1], James Hollingsworth[2], Pieter Vermeesch[1], Thomas Mitchell[1], Eric Bergman[3]

[1]Department of Earth Sciences, University College London, 5 Gower Place, WC1E 6BS London, UK

[2]Univ. Grenoble Alpes, Univ. Savoie Mont Blanc, CNRS, IRD, IFSTTAR, ISTerre, 38000 Grenoble, France

[3]Global Seismological Services, Golden, CO, USA

Contents of this file

1. Text S1 to S5
2. Figures S1 to S5

Additional Supporting Information (Files uploaded separately)

1. Dataset S1. Displacement profiles - fault-parallel movement (ew-displacement).
2. Dataset S2. Displacement profiles - fault-perpendicular movement (ns-displacement).
3. Dataset S3. Displacement profiles - vertical movement (dz-dispalcement).

Introduction The supporting information contains detailed explanations of the method used in this study (Text S1 to S5), 5 figures to illustrate the methodology and outcomes,

and additional supporting information (Dataset S1 to S3) which contain 105 displacement profiles collected along the Red Canyon Fault. Dataset S1 to S3 show our interpretation of the displacement from the stacked profiles.

Text S1. Eliminating radiometric noise in the vertical displacement map The interaction of the light with the vegetation creates radiometric noise that becomes more prominent with increasing image resolution, due to the increasing sensitivity to spatial wavelengths associated with the vegetation cover; the rough surface of this cover interacts strongly with the incoming light. Therefore, differences in the illumination conditions between pre- and post-images results in a shift in the shadow content between both images, and which varies, in part, as a function of the topographic slope and aspect of the local topography, and sun elevation and azimuth at the time of acquisition (e.g., Lacroix et al., 2019). These shifting shadows span a range of frequencies which strongly impact the correlation, thereby producing a bias in the final displacement map. We mitigate the impact of radiometric noise on the final correlation map by using a random forest algorithm (Breiman, 2001) to learn the relationship between radiometric correlation bias, pre and post image reflectance, and local topographic slope and aspect. We train the model using data taken far from the deforming area, or, when this is not possible, using high-pass filtered values. The model is then used to predict the radiometric noise component for displacement values located within the deforming region. Removal of this noisy component thus increases the signal-to-noise ratio of the tectonic component of displacement. This simple approach significantly reduces radiometric and topographic artifacts in the final displacement maps.

Text S2. Displacement measurements The along-strike fault offsets were calculated using stacked fault-perpendicular profiles taken regularly along strike of the Red Canyon fault (the signal-to-noise ratio of the Hebgen Fault displacement profiles was too low to characterize the along-strike displacement with confidence). We extracted individual profiles using COSI-Corr (Leprince et al., 2007) as fault-parallel and fault-perpendicular measurements of the surface displacement. The individual profiles were rotated to achieve an E-W alignment (Fig. S2-a). To calculate the displacement we fit a linear model to the footwall and hangingwall values between manually selected points p1 and p2 (Fig. S2-b), and p3 and p4 (which were kept constant). The tectonic offset is calculated as a difference between the linear extrapolation of the footwall and hanging wall measurements. Precision was estimated in two ways, first by standard error propagation of the least squares fit, and second by Monte Carlo simulation. Both approaches give similar results (Fig. S2-c).

Text S3. Fault displacement measurements and comparison of the OIC data with the existing offst measurements Summary of the along-strike offset measurements collected along the Red canyon fault.

Text S4. Off-fault deformation in relation to the fault geometry and topography

Text S5. Calibrated Relocations A relocation analysis of the Hebgen Lake sequence was conducted using a multiple-event relocation methodology that is optimized to yield hypocenters that are considered "calibrated", meaning that they suffer from a minimal amount of the systematic location bias intrinsic in most standard earthquake catalogs and that uncertainties in hypocentral parameters are realistic. The methodology (based on a program called "mloc") has been developed over the past two decades

and applied to relocation studies of hundreds of seismic clusters (both earthquake and nuclear explosions sources) as presented in the Global Catalog of Calibrated Earthquake Locations (GCCEL) hosted at a website operated by the U.S. Geological Survey (https://doi.org/10.5066/P95R8K8). The website also contains full documentation of the mloc software, it's use, the source code and necessary data files to set up an installation of mloc. This methodlogy was utilized in numerous published studies (e.g Pousse-Beltran et al., 2020; Karasözen et al., 2019; Nealy et al., 2017; McNamara et al., 2015).

Our relocation study included the 1959 Hebgen Lake mainshock and 5 of the larger aftershocks. The analysis was done in three main steps, in order to investigate possible problems from combining a set of relatively old readings for the 1959 sequence with that of modern events. It is often the case in such circumstances that changes through time in the constellation of observing seismograph stations creates numerical instabilities in the inversion that implements the multiple event relocation.

We first relocated these six events as a cluster to obtain an initial result for their relative locations, based on the observing stations available at the time. This cluster is uncalibrated because the arrival time data set contains only two observations at less than 4° epicentral distance. The absolute location of the cluster was based on fitting teleseismic P arrivals to the ak135 global travel-time model. The first 4 aftershocks (all on August 18) lie 10-25 km to the east of the mainshock epicenter. The last aftershock, a day later, lies 30 km to the west.

Next we relocated only the 1959 mainshock in a cluster with the modern events. The 1959 mainshock is connected to the modern cluster through 59 observations in common (out of 736 readings in total), far less than it shared in common with its own aftershocks,

but the azimuthal coverage of those observations is adequate. In addition to the 1959 mainshock the calibrated cluster includes 22 events from 1964-2020, ten of which (starting in 1998) have most of the 276 local distance (less than 1.5°) Pg and Sg readings used to locate the hypocentroid of the cluster, which determines the absolute location of the cluster in space and time.

A simple layered crustal model, perturbed from the ak135 global model, is used to calculate theoretical travel times for the direct crustal arrivals (Pg and Sg) and the Moho-refracted arrivals (Pn and Sn).

Finally we added the five aftershocks from 1959 to the calibrated cluster. The critical question is whether there are enough observations in common between these smaller 1959 events and the modern ones to adequately constrain their relative locations within the larger cluster. Even though the 1959 events behaved well when treated as a cluster by themselves and the mainshock by itself appears to be adequately connected with the modern cluster, it is not assured that the smaller events from 1959 will remain stable when added to the modern cluster. The question is answered in the inversion process, which will have difficulty converging if any of the events in the cluster are inadequately "connected" to the rest of the cluster. In fact, we did observe convergence problems after adding the 1959 aftershocks to the cluster, generally with the locations of all six of the 1959 events failing to converge. In some runs the inversion would converge successfully but in a subsequent run, after a minor change to the dataset or weighting, it would fail again. With experimentation it was found that two of the 1959 aftershocks were the main cause of the convergence problems, so the final runs to obtain calibrated locations for the cluster were done without those two events.

The difference in the location of the mainshock when calibrated with modern events and 1959 aftershocks is negligible; when the four 1959 aftershocks are included the mainshock epicenter is 1 km south of the location when they are not. The uncertainty of the mainshock epicenter is smaller, by ∼0.5 km, when the aftershocks are included. The calibrated locations of the 1959 events are:

1 1959 8 18 6 37 14.15 44.8114 -111.1883 12.0

2 1959 8 18 7 56 16.62 44.7699 -110.8601 10.0

3 1959 8 18 8 41 46.82 44.8115 -111.0715 10.0

4 1959 8 18 15 26 6.09 44.8446 -110.8096 10.0

Because the connectivity of the 1959 sequence, especially the aftershocks, with the modern events in the cluster is evidently weak the true uncertainty of the these epicenters is probably larger than the calculated uncertainties (1.7-2.3 km), perhaps by several km. **Data Set S1.** The fault-parallel displacement profiles extracted from the E-W displacement map.

Data Set S2. The fault-perpendicular displacement profiles extracted from the N-S displacement map.

Data Set S3. The profiles showing the vertical displacement extracted from the DEM differencing.

References

Breiman, L. (2001). Random forests. *Machine learning*, *45*(1), 5–32.

Doser, D. I. (1985). Source parameters and faulting processes of the 1959 Hebgen Lake, Montana, earthquake sequence. *Journal of Geophysical Research: Solid Earth*, *90*(B6), 4537–4555.

Johnson, K. L., Nissen, E., & Lajoie, L. (2018). Surface rupture morphology and vertical slip distribution of the 1959 M w 7.2 Hebgen Lake (Montana) earthquake from airborne lidar topography. *Journal of Geophysical Research: Solid Earth*, *123*(9), 8229–8248.

Karasözen, E., Nissen, E., Bergman, E. A., & Ghods, A. (2019). Seismotectonics of the zagros (iran) from orogen-wide, calibrated earthquake relocations. *Journal of Geophysical Research: Solid Earth*, *124*(8), 9109–9129.

Lacroix, P., Araujo, G., Hollingsworth, J., & Taipe, E. (2019). Self-entrainment motion of a slow-moving landslide inferred from landsat-8 time series. *Journal of Geophysical Research: Earth Surface*, *124*(5), 1201–1216.

Leprince, S., Barbot, S., Ayoub, F., & Avouac, J.-P. (2007). Automatic and precise orthorectification, coregistration, and subpixel correlation of satellite images, application to ground deformation measurements. *IEEE Transactions on Geoscience and Remote Sensing*, *45*(6), 1529–1558.

McNamara, D. E., Benz, H. M., Herrmann, R. B., Bergman, E. A., Earle, P., Holland, A., ... Gassner, A. (2015). Earthquake hypocenters and focal mechanisms in central oklahoma reveal a complex system of reactivated subsurface strike-slip faulting. *Geophysical Research Letters*, *42*(8), 2742–2749.

Nealy, J. L., Benz, H. M., Hayes, G. P., Bergman, E. A., & Barnhart, W. D. (2017). The 2008 wells, nevada, earthquake sequence: Source constraints using calibrated multiple-event relocation and insar. *Bulletin of the Seismological Society of America*, *107*(3), 1107–1117.

Pousse-Beltran, L., Nissen, E., Bergman, E. A., Cambaz, M. D., Gaudreau, É.,

Karasözen, E., & Tan, F. (2020). The 2020 m w 6.8 elazığ (turkey) earthquake reveals rupture behavior of the east anatolian fault. *Geophysical Research Letters*, *47*(13), e2020GL088136.

Witkind, I. J. (1964). *Reactivated faults north of Hebgen Lake*. US Government Printing Office.

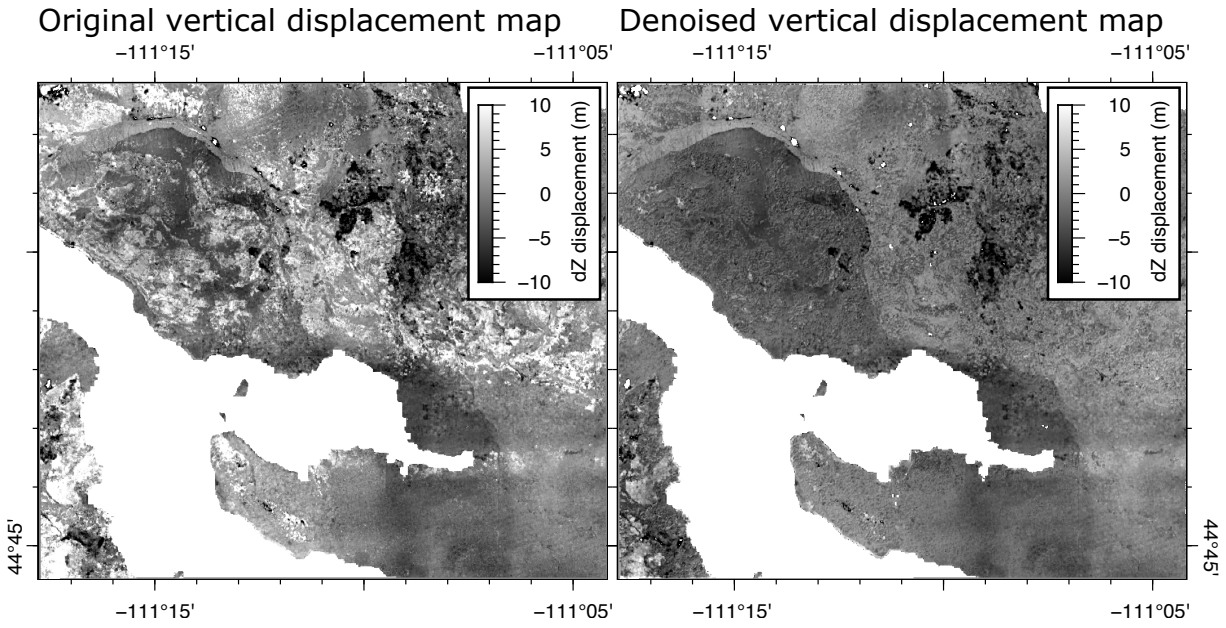

Figure S1. The image shows a vertical displacement map before and after the correction for radiometric noise was applied.

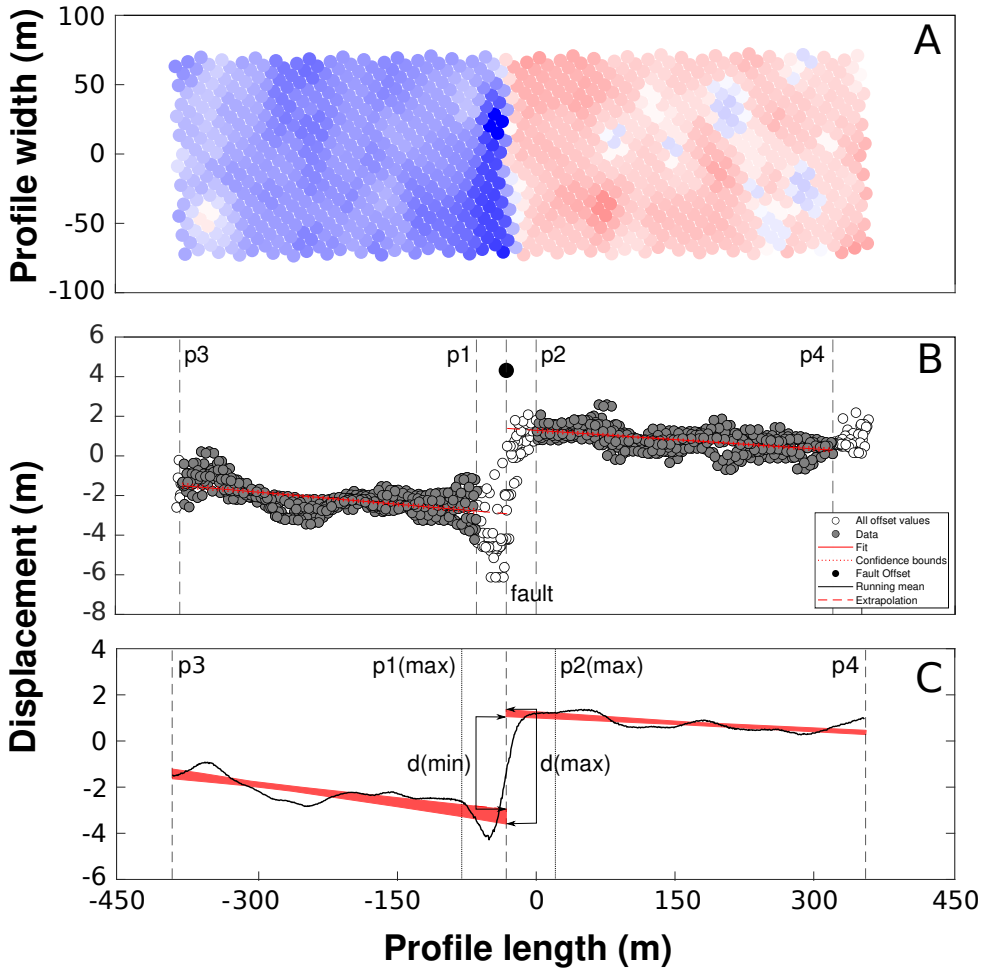

Figure S2. (a) The stacked profile of the fault-perpendicular offset determined by optical image correlation. (b) The same profile shown in 2 dimensions, with distance set out along the x-axis against displacement magnitude along the y-axis. p1, p2, p3 and p4 are the bounds of the data used for the linear extrapolation. (c) The running mean (black line) of the data displayed in (a) and (b). The p1 and p2 anchors were selected from the area between p1(max) and the fault, and p2(max) and the fault, respectively. The red uncertainty band for the offset measurements was obtained by Monte Carlo simulation.

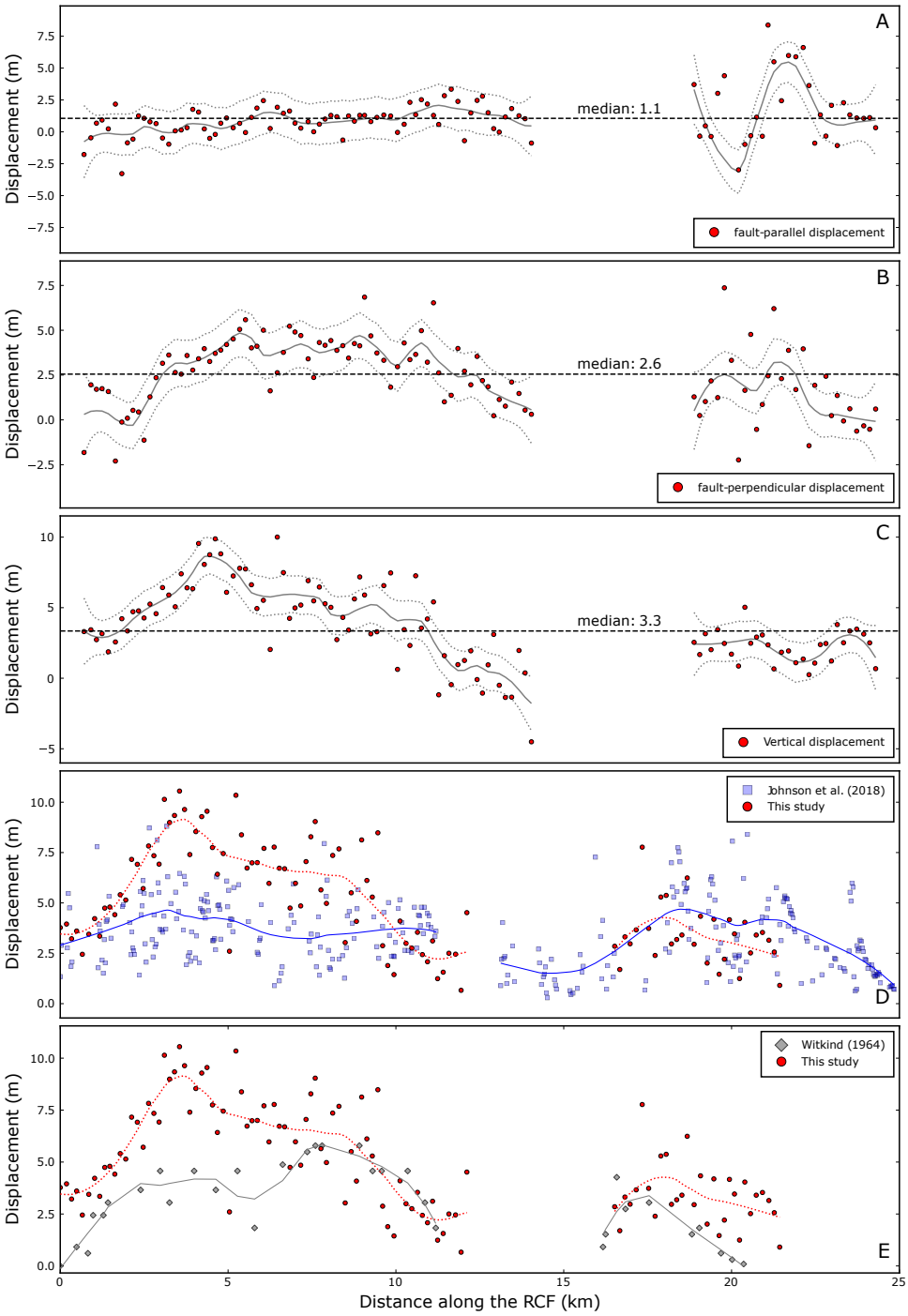

Figure S3. (a) Fault-parallel, (b) fault-perpendicular and (c) vertical offset measurements determined from the stacked profiles which were extracted from the correlation maps. (d) and (e) show the comparison of the offset measurements calculated in this study with the existing estimates from the LiDAR (Johnson et al., 2018) and filed (Witkind, 1964) studies.

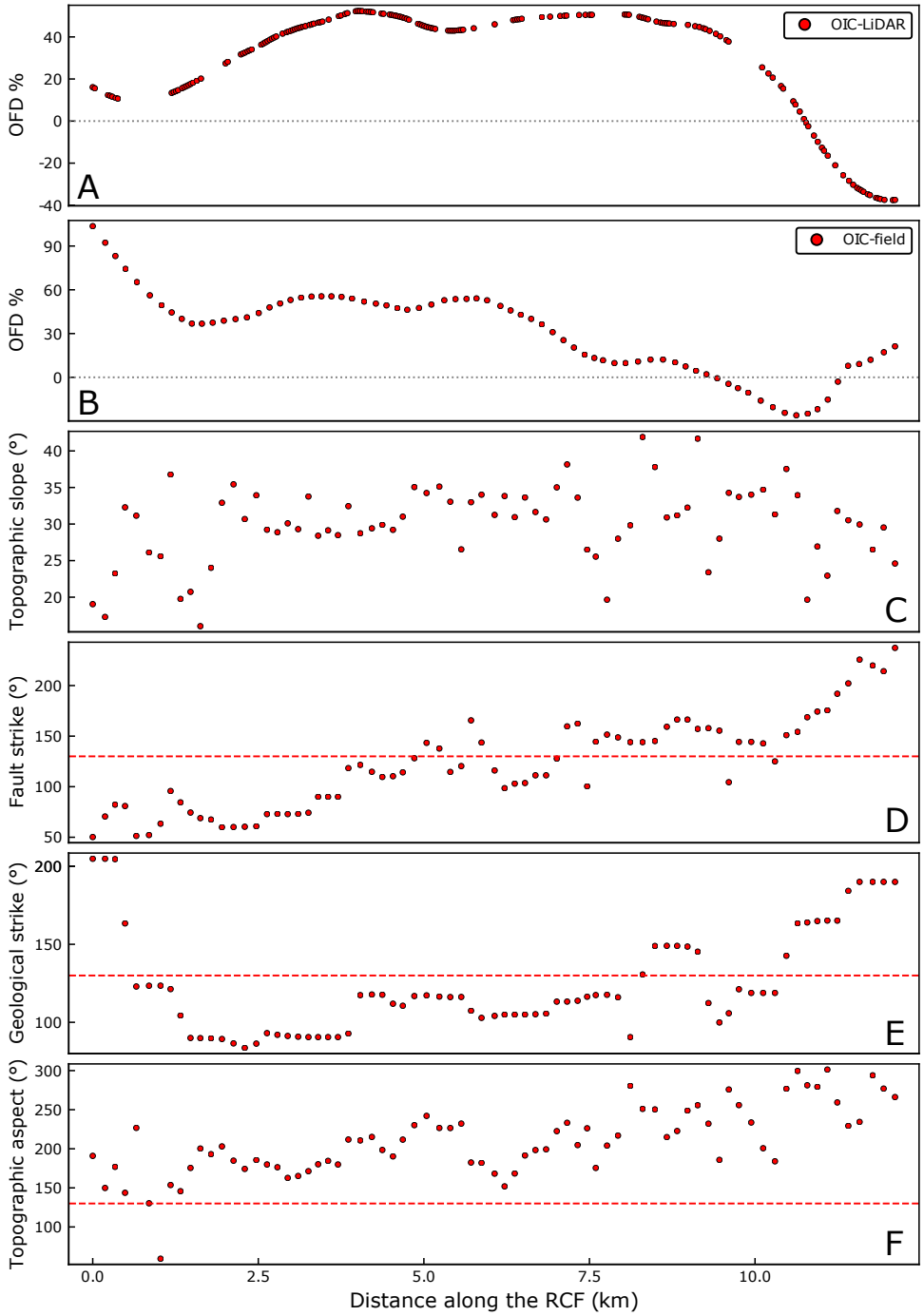

Figure S4. The relationship between the geometric characteristics of the topography, geology and distributed off-fault deformation. Grey dotted line in (a) and (b) is centered at 0; red dashed line in (d), (E) and (f) shows the direction of the fault plane (130° ±10°)(Doser, 1985). We calculated the percentage of the off-fault damage from the offset estimates calculated in this study and A) LiDAR (Johnson et al., 2018) and B) field (Witkind, 1964) displacement measurements. The observation suggest that large %OFD is related to the orientation of the geological strike (e) and strike of the fault (d) while slope (c) and aspect (f) of topography appear to have no effect on the distribution of the

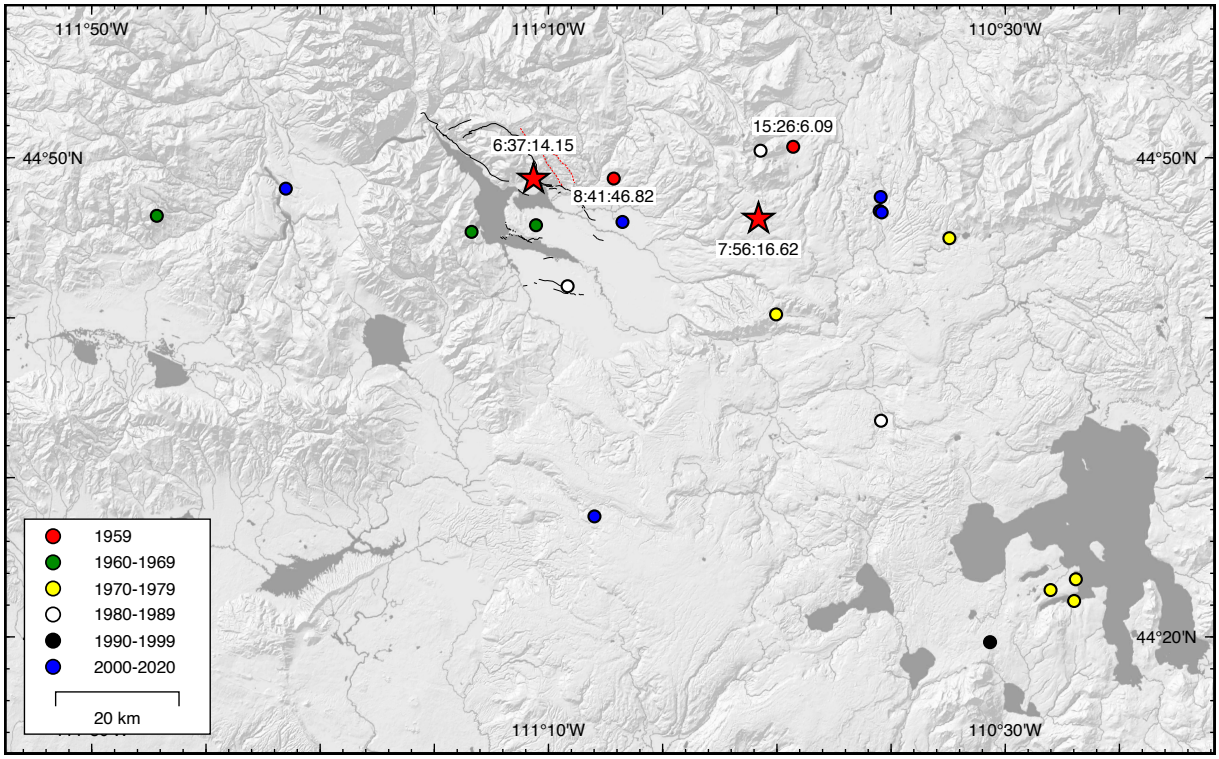

Figure S5. The the calibrated earthquake relocations from the Hebgen Lake and Yellowstone regions. The 1959 events are red, the star symbols are the two sub-events of the main-shock.